Integrative Biology

PAPER

Cite this: *Integr. Biol.*, 2016, 8, 1232

Stiffness of pancreatic cancer cells is associated with increased invasive potential†

Angelyn V. Nguyen,[a] Kendra D. Nyberg,[ab] Michael B. Scott,[a] Alia M. Welsh,[c] Andrew H. Nguyen,[d] Nanping Wu,[d] Sophia V. Hohlbauch,[e] Nicholas A. Geisse,[e] Ewan A. Gibb,[f] A. Gordon Robertson,[f] Timothy R. Donahue[dg] and Amy C. Rowat*[abg]

Received 16th July 2016,
Accepted 7th October 2016

DOI: 10.1039/c6ib00135a

www.rsc.org/ibiology

Metastasis is a fundamentally physical process in which cells are required to deform through narrow gaps as they invade surrounding tissues and transit to distant sites. In many cancers, more invasive cells are more deformable than less invasive cells, but the extent to which mechanical phenotype, or mechanotype, can predict disease aggressiveness in pancreatic ductal adenocarcinoma (PDAC) remains unclear. Here we investigate the invasive potential and mechanical properties of immortalized PDAC cell lines derived from primary tumors and a secondary metastatic site, as well as noncancerous pancreatic ductal cells. To investigate how invasive behavior is associated with cell mechanotype, we flow cells through micron-scale pores using parallel microfiltration and microfluidic deformability cytometry; these results show that the ability of PDAC cells to passively transit through pores is only weakly correlated with their invasive potential. We also measure the Young's modulus of pancreatic ductal cells using atomic force microscopy, which reveals that there is a strong association between cell stiffness and invasive potential in PDAC cells. To determine the molecular origins of the variability in mechanotype across our PDAC cell lines, we analyze RNAseq data for genes that are known to regulate cell mechanotype. Our results show that vimentin, actin, and lamin A are among the most differentially expressed mechanoregulating genes across our panel of PDAC cell lines, as well as a cohort of 38 additional PDAC cell lines. We confirm levels of these proteins across our cell panel using immunoblotting, and find that levels of lamin A increase with both invasive potential and Young's modulus. Taken together, we find that stiffer PDAC cells are more invasive than more compliant cells, which challenges the paradigm that decreased cell stiffness is a hallmark of metastatic potential.

Insight, innovation, integration

Pancreatic ductal adenocarcinoma (PDAC) cells sense and respond to the increased stiffness of their microenvironment and deform through narrow gaps during metastasis. While physical processes are implicated in the progression of PDAC, the mechanical phenotype, or mechanotype, of tumor cells is poorly understood. Here we show that stiffer PDAC cells have a greater invasive potential than more deformable cells. We also investigate mechanoregulating proteins that contribute to the variability in mechanotype that we observe across different PDAC cell lines. Taken together, our findings provide insight into the mechanome of PDAC cells and suggest that the current paradigm of cell deformability as a hallmark of metastatic potential depends on cancer type.

Introduction

Pancreatic ductal adenocarcinoma (PDAC) remains one of the most aggressive and lethal cancers.[1,2] A major factor in the progression of this disease is the interaction between tumor cells and their microenvironment.[3,4] For example, mechanical cues activate signalling pathways, such as the JAK-STAT3 and integrin-FAK-ROCK axes, which promote cancer by triggering a positive feedback loop that results in increased ECM deposition,[4] fibrosis, and stiffness of the extracellular matrix (ECM).[5] In turn, cells respond to the stiffness of their substrate

[a] *Department of Integrative Biology and Physiology, University of California, Los Angeles, USA. E-mail: rowat@ucla.edu*
[b] *Department of Bioengineering, University of California, Los Angeles, USA*
[c] *Department of Microbiology, Immunology, and Molecular Genetics, University of California, Los Angeles, USA*
[d] *Department of General Surgery, University of California, Los Angeles, USA*
[e] *Asylum Research, an Oxford Instruments Company, Santa Barbara, California, USA*
[f] *Canada's Michael Smith Genome Sciences Centre, British Columbia Cancer Agency, Vancouver, BC, Canada*
[g] *Jonsson Comprehensive Cancer Center, University of California, Los Angeles, USA*
† Electronic supplementary information (ESI) available. See DOI: 10.1039/c6ib00135a

by altering their mechanical phenotype,[6,7] or mechanotype. A deeper knowledge of PDAC cell mechanotype and its underlying molecular components would provide a more complete understanding of how cells sense and transduce mechanical cues, and may ultimately identify molecules in mechanosignaling pathways that could be targeted to impede disease progression.

Cell mechanotype is linked to invasive potential in several types of cancers, including breast and ovarian.[8–10] The current paradigm is that more invasive or metastatic cancer cells are more deformable than their benign or less invasive counterparts.[8–17] A more deformable cell may have a selective advantage for metastasis, which requires individual tumor cells to transit through narrow vessels of the vasculature and extravasate to secondary tumor sites. However, there is also evidence that stiffer cancer cells are more invasive. For example, stiffer lung cancer cells and transformed fibroblasts are more motile in *in vitro* invasion assays.[18,19] While metastasis is the leading cause of death in PDAC and invasion is linked to cell mechanical properties in other cancers, the mechanotype of PDAC cells is not well understood.

Since metastasis requires cells to invade through the extracellular matrix and deform during transit through the vasculature, studies aiming to understand the possible roles of cell deformability in PDAC can benefit from complementary methods that measure cells in attached and suspended states. The use of multiple methods can also provide insight into the molecular mechanisms that determine cell mechanotype: different methods enable deformations over varying length scales, which determine the subcellular structures that contribute to the deformation response. For example, fluidic methods, such as micropipette aspiration and microfluidic deformability cytometry, measure cells in a suspended state, where cortical actin[20] and the nucleus[21,22] contribute to the deformation of cells through micron-scale pores. By contrast, in methods that induce local, 10 nm to 1 μm deformations on cells adhered to their substrate, such as atomic force microscopy (AFM)[23] and magnetic twisting cytometry,[24] actin can organize into stress fibers,[25] which have a marked effect on cell stiffness. Adhered cells also generate traction stresses, which result in increased cell stiffness[26] and enhanced invasive behavior of cancer cells.[27] For all of these reasons, comparisons of the same types of PDAC cells using multiple, complementary methods should provide more detailed insights into cancer cell mechanotype.

Here we investigate the invasive behavior and mechanotype of four immortalized pancreatic ductal cell lines, including cell lines derived from primary PDAC malignancies (MIA PaCa-2 and PANC-1) and a metastatic pleural effusion (Hs766T), as well as a nontransformed control cell line (HPDE). While the PDAC cell lines in our panel are derived from different sites, they all have similar founder mutations,[28] including alterations in *KRAS*, *TP53*, and *P16*. To determine the invasive potential of these cells, we perform a modified scratch wound invasion assay with Matrigel overlay to simulate the ECM. We also use a transwell migration assay without Matrigel to probe how effectively cells can migrate through narrow gaps independently of proteolytic matrix degradation. To assess how the deformability of PDAC cells is associated with their invasive potential, we use complementary mechanotyping methods to measure cells in both suspended and adhered states. We use parallel microfiltration (PMF)[15] and single-cell microfluidic deformability cytometry[29] to measure the deformability of suspended cells, and atomic force microscopy (AFM) to determine the Young's modulus of adhered cells. By analyzing gene expression data across our 3 PDAC cell lines, as well as data from 38 additional PDAC cell lines, we identify lamin A as a possible mechanoregulating protein that may contribute to the variability we observe in pancreatic ductal cell mechanotype. Taken together, our results show that stiffer PDAC cells are more invasive than more compliant PDAC cells, demonstrating that the relationship between cell invasive potential and mechanotype may vary for different types of cancers.

Results

Invasive behavior varies across pancreatic ductal adenocarcinoma cell lines

As cell mechanotype is associated with the invasive potential of cancer cells,[8–10] we first determine the invasion efficiency of PDAC cells derived from both primary and secondary sites, as well as that of noncancerous pancreatic ductal cells. To quantify cell invasion, we measure wound confluence using a modified scratch wound invasion assay where cells are overlaid with a ~1.5 mm-thick layer of Matrigel, a protein mixture that recapitulates the ECM (Fig. 1B); this setup requires cells to invade through a 3D matrix.[30,31] Our results show that there is variability in how quickly pancreatic ductal cells move into the wound gap. At 72 hours, the wound confluence across PDAC cells lines varies from 33 to 60% (Fig. 1A and B), indicating that cells with similar founder mutations[28] (Table S1, ESI†) have different invasion efficiencies. The MIA PaCa-2 and PANC-1 cells, which are derived from primary tumors, show increased invasion compared to the noncancerous HPDE cells (MIA PaCa-2: 33 ± 1%, PANC-1: 40 ± 2%, HPDE: 22 ± 4%; $p_{\mathrm{MIA–HPDE}} = 8.5 \times 10^{-2}$, $p_{\mathrm{PANC–HPDE}} = 3.5 \times 10^{-3}$). PANC-1 cells also show a significantly greater wound confluence than MIA PaCa-2 cells ($p_{\mathrm{MIA–PANC}} = 4.0 \times 10^{-2}$). The Hs766T cells, which are derived from metastatic pleural effusion, exhibit the greatest invasive potential with a wound confluence of 60 ± 5%, which is ~2-fold higher than both the PANC-1 ($p_{\mathrm{Hs766T–PANC}} = 5.8 \times 10^{-3}$) and MIA PaCa-2 cells ($p_{\mathrm{Hs766T–MIA}} = 9.9 \times 10^{-4}$).

Since the speed at which cells migrate on a 2D surface could influence the observed differences in invasive potential, we repeat the scratch wound migration assays without a 3D Matrigel matrix (Fig. S1, ESI†). These results show that the cancerous cell lines have a significantly lower wound confluence than the HPDE cells after 24 hours (HPDE: 86 ± 6%, PDAC cell lines: 29 ± 4% to 34 ± 6%; $p_{\mathrm{HPDE–PDAC}} < 3.6 \times 10^{-3}$), but there are no significant differences in migration efficiency between PDAC cell lines ($p > 0.05$ for all pairwise comparisons). Overall, we observe no significant correlation between migration and invasion potential ($R = -0.15$), indicating that our modified scratch wound invasion assay does not simply reflect differences in cell motility.

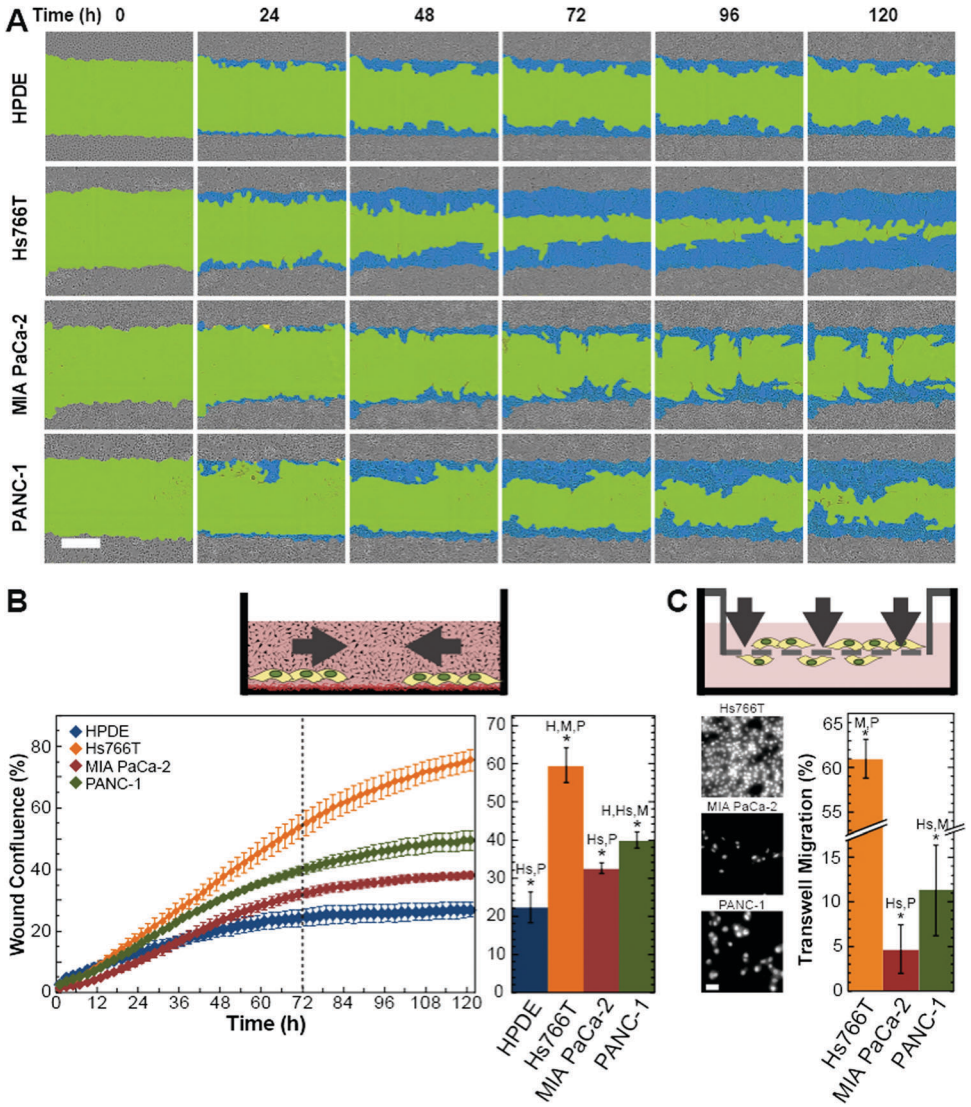

Fig. 1 Invasive behavior of pancreatic ductal adenocarcinoma cell lines. (A) Time series of images showing scratch wound invasion of pancreatic ductal cells through Matrigel. Wound confluence is the percentage of wound area covered by cells. Color legend: green is the wound area, blue shows wound confluence in the wound area, and grey represents the confluent cells outside of the wound area. Scale, 300 μm. (B) Schematic illustration showing the modified scratch wound assay. Cells are plated on a layer of thin Matrigel and invade into the thick 3D matrix of overlaid Matrigel that fills the scratch wound. The line plot shows quantification of wound confluence over time. The dotted line indicates the 72 h time point, which we use to compare wound confluence values for statistical significance. The bar plot represents wound confluence at the 72 h time point. Pairwise p-values are determined by a Student's t-test. *$p < 0.05$. (C) Schematic illustration showing the transwell migration assay. Cells migrate through the 8 μm pores of a polycarbonate membrane in response to a chemoattractant on the opposite side of the membrane. Images of transwell migration assays showing DRAQ5-labeled nuclei of cells that migrate through the 8 μm pores of a polycarbonate membrane after 12 hours. Scale, 50 μm. Pairwise p-values are determined by a Student's t-test. *$p < 0.05$. All error bars represent standard errors. The significance of pairwise comparisons between cell lines is shown in panels B and C by the initial(s) of the cell lines that are significantly different where H: HPDE, Hs: Hs766T, M: MIA PaCa-2, and P: PANC-1. For example, in panel B, HPDE is significantly different (*$p < 0.05$) from Hs766T (Hs) and PANC-1 (P).

Cell proliferation can also impact wound confluence. To exclude cell proliferation as a factor in our invasion results, we track the density of pancreatic ductal cell lines over 120 hours by time-lapse imaging (Fig. S2A–C, ESI†). We find that the Hs766T cells, which are the most invasive, have the lowest confluence of the four pancreatic ductal cell lines at 72 hours (47 ± 2%), indicating that these cells have the slowest proliferation rate. Conversely, the MIA PaCa-2 cells, which are the slowest PDAC cells to invade, show the highest confluence, which indicates that they proliferate most quickly. Across our 3 pancreatic cell lines, proliferation does not correlate with cell invasive potential ($R = -0.097$). We also track the proliferation of cells overlaid with Matrigel, as in our invasion assay (Fig. S2D and E, ESI†). We find that there is only a ~4–6% difference in proliferation across PDAC cell lines after 72 h. By contrast, we observe up to a 27% difference in invasion at the same time point (Fig. 1A and B). Furthermore, while apoptosis could influence differences in measurements of cell invasion,

we observe no significant differences in apoptosis across PDAC cell lines with Matrigel overlay (Fig. S3, ESI†). Taken together, these results indicate that differences in cell doubling rates across our cell lines cannot explain the differences in invasion efficiencies that we observe.

PDAC cell migration through membrane pores is consistent with invasion through Matrigel

Invasion depends on the ability of cells to deform through narrow gaps, as well as their ability to degrade the surrounding protein matrix with secreted matrix metalloproteases (MMPs).[32–34] Degradation of the ECM results in an increased pore size, which can enhance invasion.[35] Thus, the variable expression and activity of secreted MMPs across PDAC cell lines[36–38] could influence our measurements of cell invasion through a protein matrix. To assess the contribution of cell deformability to invasion independently of MMP activity, we use a transwell migration assay, in which cells must actively deform through pores of a polycarbonate membrane. After 12 hours, MIA PaCa-2 cells have a lower percent migration than PANC-1 cells (MIA PaCa-2: 5 ± 3%, PANC-1: 11 ± 5%; $p = 1.1 \times 10^{-16}$), while the Hs766T cells show a statistically higher transwell migration efficiency compared to the two other PDAC cells (Hs766T: 62 ± 5%; $p_{\text{Hs766T–MIA}} = 2.0 \times 10^{-6}$, $p_{\text{Hs766T–PANC-1}} = 2.4 \times 10^{-6}$) (Fig. 1C). These transwell migration data are consistent with the data from our modified scratch wound invasion assay with Matrigel ($R = 0.99$; Fig. 5 and Table S2, ESI†), indicating that the variations in PDAC invasive potential are consistent with the ability of cells to migrate through narrow gaps.

PDAC cells vary in their ability to passively deform through micron-scale pores

During metastasis, cells must deform through micron-scale gaps in the ECM and basement membrane. Since more invasive cancer cells are generally more deformable than less invasive cells,[8–10] we next ask whether the differences in invasive potential between cell lines can be attributed to differences in the ability of cells to passively deform through pores. Here we refer to 'deformability' as the ability of cells to flow through pores when driven by an applied pressure.

To measure the deformability of pancreatic ductal cells, we use parallel microfiltration (PMF).[15] In PMF, we flow a suspension of cells across a porous membrane by applying air pressure for a defined time and then quantify the retention, or the volume of fluid that is retained above the membrane. Higher retention indicates that a larger fraction of cells has occluded the pores. In contrast, lower retention indicates that cells can passage more easily through the pores and thereby enable more fluid to flow across the membrane. Prior to PMF, cell suspensions are filtered through a 35 μm mesh filter to reduce aggregates; we confirm that our samples contain over 98% single cells using image analysis (Fig. S4, ESI†). MIA PaCa-2 cells exhibit a lower retention of 40 ± 10% compared to the HPDE noncancerous control cells (HPDE: 57 ± 7%, $p_{\text{MIA–HPDE}} = 8.0 \times 10^{-4}$) (Fig. 2A). In contrast, the PANC-1 cells exhibit a significantly increased retention (88 ± 8%) compared to both the noncancerous control ($p_{\text{PANC–HPDE}} = 2.0 \times 10^{-5}$) and the MIA PaCa-2 cells ($p_{\text{PANC–MIA}} = 1.2 \times 10^{-7}$). The Hs766T cells show a marginally higher retention than the HPDE control cells (Hs766T: 60 ± 11%, $p_{\text{Hs766T–HPDE}} = 5.5 \times 10^{-2}$).

Since the ability of cells to occlude pores can depend on both cell deformability and cell size, we next measure the size of cells in suspension using imaging flow cytometry (Fig. S5A and B, ESI†) and plot percent retention as a function of cell diameter (Fig. 2B). Overall, we observe that there is a positive correlation between retention and cell size ($R = 0.72$), indicating that cell size could influence retention. While the observed relationship between cell size and retention may explain the higher retention of the larger PANC-1 cells, the other pancreatic ductal cell lines have similar size distributions yet show significant differences in retention. For example, the MIA PaCa-2 have a slightly larger size compared to the Hs766T cells, yet exhibit a significantly lower retention, which indicates that these cells occlude fewer pores and are therefore more deformable. In addition to cell size, nuclear size can also impact occlusion of pores and channels.[21,22] The median diameter of nuclei in our pancreatic ductal cells is 11–16 μm (Fig. S5A and C, ESI†), suggesting that some nuclear deformation is also required for cells to deform through micron-scale pores. We observe moderate correlations between nuclear size and transit time ($R = 0.86$), as well as nuclear size and retention ($R = 0.62$). However, there is a very strong correlation between cell and nuclear size ($R = 0.99$ for cells in suspension). Therefore, our cell deformability measurements by PMF and microfluidic deformability cytometry could be influenced by both the cytoskeleton and nucleus.

As an independent measure of how cells transit through narrow gaps, we use microfluidic deformability cytometry. This method enables us to measure the timescale, or transit time, for single cells to deform through micron-scale channels while simultaneously characterizing their size. Cells that have larger elastic moduli tend to have longer transit times.[29,39] When considering the entire population, the PANC-1 cells have a similar median transit time as the HPDE control (bootstrapped median transit time ± confidence interval, PANC-1: 18 ± 5.3 ms, HPDE: 18 ± 2.0 ms; $p_{\text{PANC–HPDE}} = 2.8 \times 10^{-2}$). Consistent with our retention data, the MIA PaCa-2 cells have a lower transit time compared to the HPDE cells (MIA PaCa-2: 4.0 ± 0.0 ms, $p_{\text{MIA–HPDE}} \approx 0.0$), substantiating that these cells are more deformable than the noncancerous controls. In addition, we observe that the Hs766T cells have significantly lower median transit times than the HPDE cells (Hs766T: 4.8 ± 0.5 ms, $p_{\text{HPDE–Hs766T}} \approx 0.0$).

To determine the role of cell size in transit time, we gate for cells of a similar size and compare their transit time distributions (Fig. S6, ESI†). Here we focus our analysis on the size bins of the largest (PANC-1) and smallest (Hs766T) cells of our panel. For example, we first compare transit time distributions for cells that are within 5 μm of the PANC-1 median cell size of 24 μm (Fig. S6D, ESI†). While the non-gated data show that PANC-1 and HPDE cells have similar median transit times across the entire population (Fig. 2C and D), our size-gated data reveal that the PANC-1 cells have a shorter median transit time than HPDE cells (PANC-1: 19 ± 8.5 ms, HPDE: 26 ± 5.0 ms; $p_{\text{PANC–HPDE}} = 4.8 \times 10^{-6}$), suggesting that PANC-1 cells are more deformable than the HPDE control cells when accounting for differences in cell size.

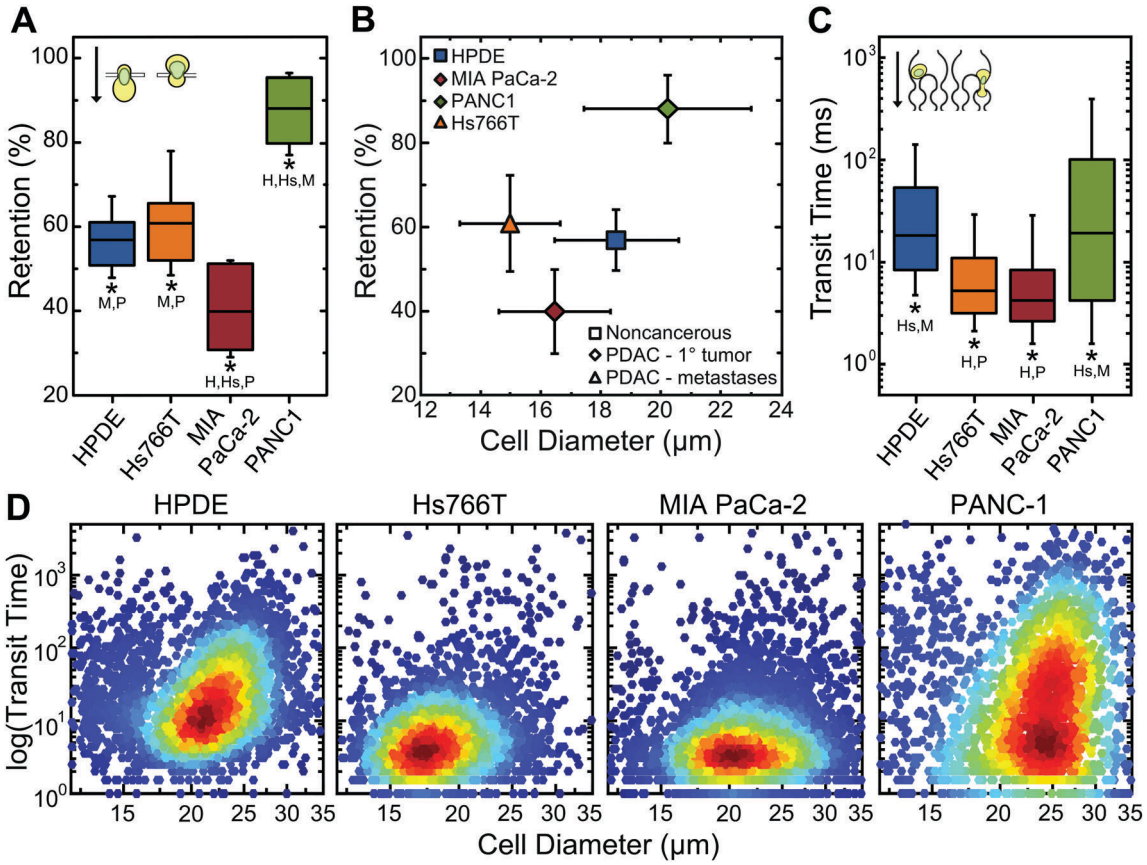

Fig. 2 Deformability of pancreatic ductal cells. (A) Retention as measured by parallel microfiltration (PMF). A suspension of cells that more effectively occludes the 10 μm pores of the membrane in response to external air pressure will exhibit a higher retention. Inset shows schematic of cells passing through a porous membrane. Boxes represent the 25th and 75th percentiles, whiskers represent the 10th and 90th percentiles, and horizontal lines represents the means. (B) Retention as a function of cell diameter. Data points represent the means and the error bars represent the standard deviations for both axes. (C) Transit time is measured using microfluidic deformability cytometry and reveals the timescale required for single cells to deform through a channel with a 9 μm × 10 μm diameter, as illustrated in the inset. Cells that are less deformable have longer transit times than cells that are more deformable. For each cell line, $n > 2200$ cells. Boxes represent the 25th and 75th percentiles, whiskers represent the 10th and 90th percentiles, and horizontal lines represent the bootstrapped medians. Size-gated transit time data is shown in Fig. S6 (ESI†). (D) Density scatterplots show the transit time of single cells as a function of cell size. Statistical significance of the deformability cytometry results is calculated using a Mann–Whitney *U* test. All other statistical significances is calculated with a Student's *t*-test. *p-value < 0.05. The significance of pairwise comparisons between cell lines is shown in panels A and C by the initial(s) of the cell lines that are significantly different where H: HPDE, Hs: Hs766T, M: MIA PaCa-2, and P: PANC-1. For example, in panel A, HPDE is significantly different (*$p < 0.05$) from MIA PaCa-2 (M) and PANC-1 (P).

Since the Hs766T cells are significantly smaller than the HPDE cells (Fig. 2D and Fig. S5A, B, ESI†), we also compare transit time distributions across cell lines within the median size range of the Hs766T cells (18.3 ± 2.5 μm) (Fig. S6B, ESI†). Our results show that even for cells of similar sizes, the Hs766T cells have a significantly reduced transit time (Hs766T: 4.8 ± 0.5, HPDE: 9.8 ± 1.5 ms; $p_{\text{HPDE–Hs766T}} = 1.2 \times 10^{-67}$), indicating that these cells are more deformable than the noncancerous HPDE cells. Thus, while both cell size and deformability can impact how cells deform through narrow gaps, our size-gated data show that even for cells of similar size, there are differences in transit time, reflecting the variability in cell mechanotype across our PDAC cell lines, both within and between populations. Collectively, our fluidic assays show that the MIA PaCa-2 cells passively deform through narrow gaps most readily, as indicated by their low retention and transit time. Interestingly, while the MIA PaCa-2 cells are the most deformable, they show a slightly lower invasive potential compared to the PANC-1 cells (Fig. 1), which have higher retention and transit times. By contrast, the Hs766T cells are the most invasive but have similar transit times and increased retention compared to the MIA PaCa-2 cells. Overall, for the three PDAC cell lines tested, we observe weak correlations between PDAC cell invasive potential and the deformability of suspended cells as measured using our fluidic assays [$R_{\text{Invasion–Retention}} = 0.21$, $R_{\text{Transwell–Retention}} = 0.05$, $R_{\text{Invasion–Transit Time}} = -0.24$; $R_{\text{Transwell–Transit Time}} = -0.39$] (Fig. 5 and Table S2, ESI†). Our results contrast previous studies showing that lung, breast and ovarian cancer cells with higher invasive potential have shorter transit times[14,16] and transformed ovarian cells have a lower retention.[15]

Stiffer pancreatic cancer cells tend to be more invasive

Before cancer cells reach circulation, they adhere to fibers and other cells as they disseminate and invade into surrounding tissues.

Therefore, we next use atomic force microscopy (AFM) to measure the Young's modulus of the central cytoplasmic region of pancreatic ductal cells in an adhered state. Our data show that the MIA PaCa-2 and PANC-1 cells have significantly lower median Young's moduli than the noncancerous HPDE cells (bootstrapped mean ± confidence intervals: MIA PaCa-2: 1.7 ± 1.0 kPa, PANC-1: 2.4 ± 1.1 kPa, HPDE: 3.7 ± 1.2 kPa; $p_{\text{MIA–HPDE}} = 1.6 \times 10^{-5}$, $p_{\text{PANC–HPDE}} = 1.3 \times 10^{-3}$) (Fig. 3A–C). The PANC-1 cells show a statistically significant 1.4× increase in the average Young's modulus compared to MIA PaCa-2 cells ($p = 2.7 \times 10^{-2}$). In contrast, the Hs766T cells have an average Young's modulus that is higher than both the MIA PaCa-2 and PANC-1 cells (Hs766T: 3.0 ± 2.0 kPa; $p_{\text{Hs766T–MIA}} = 1.2 \times 10^{-4}$, $p_{\text{Hs766T–PANC}} = 5.0 \times 10^{-3}$), but similar to that of the HPDE cells ($p_{\text{Hs766T–HPDE}} = 9.7 \times 10^{-1}$) (Fig. 3C). Compared to the other pancreatic ductal cancer cell lines, the stiffer Hs766T cells have a significantly greater invasive potential (Fig. 1). These data demonstrate that pancreatic cancer cells with a higher Young's modulus are more invasive than cancer cells that are more compliant ($R_{\text{Invasion–Young's Modulus}} = 0.97$; $R_{\text{Transwell–Young's Modulus}} = 0.92$), which contrasts previous studies that show more invasive breast and ovarian cancer cells have a lower Young's modulus than their benign and less invasive counterparts.[9,10]

Lamin A is associated with variability in PDAC cell mechanotype

To investigate the molecular origins underlying the observed differences in cell mechanotype of PDAC cells, we compile a list of genes that regulate cell mechanical properties,[40–45] which we collectively refer to as the 'mechanome'. Using publicly available RNAseq data,[46] we identify mechanome genes that have the greatest differential expression across our PDAC cell lines (Fig. 4A). The four genes that exhibit the largest standard deviation are *VIM*, *ACTB*, *ACTG1*, and *LMNA*. These genes also show the highest standard deviations across a cohort of 41 PDAC cell lines (Fig. S8, ESI†). Vimentin (*VIM*) is a cytoplasmic intermediate filament protein that contributes to the mechanical properties of various cell types.[47–49] Reduced levels of vimentin are associated with decreased stiffness of mouse embryo fibroblasts[50,51] and breast cancer cells.[52] Vimentin is also a biomarker for epithelial-to-mesenchymal transition (EMT): cells with increased levels of vimentin tend to be more motile and invasive.[53] Our previous work shows that EMT-transformed ovarian cancer cells are more deformable than epithelial-type cells.[15] *ACTB* and *ACTG1* form protein products that polymerize to form filamentous (F)-actin, which is a well-established regulator of cell mechanotype and motility.[54,55] We prioritize ß-actin for further analysis, as this protein is implicated in cancer progression.[54–56] We also investigate *LMNA*, which encodes lamin A; this nuclear-specific intermediate filament protein underlies the inner nuclear membrane, and is important in essential processes including chromatin organization, gene transcription, and DNA repair.[57] Lamin A is a key determinant of the shape stability of the cell nucleus,[58] and contributes to the mechanical properties of different cell and tissue types.[21,22,45,58,59] Therefore, we focus on validating the role of vimentin, ß-actin, F-actin, and lamin A in the mechanotypic variability of our pancreatic ductal cells.

We first quantify levels of vimentin by immunoblotting, revealing that there is significant variability across cell lines (Fig. 4B and C). MIA–PaCa-2 cells have the highest levels of vimentin, which are approximately 2-fold greater than levels in PANC-1 ($p = 0.08$). By contrast, HS766T and HPDE have no detectable vimentin. While the variability in vimentin levels across the cell lines is significant, it does not appear to explain the variability that we observe in cell mechanotype and invasive behavior, as the MIA PaCa-2 cells are the most deformable of our PDAC cell lines, and cells that are deficient in vimentin are typically more deformable.[50–52]

Our data show that ß-actin levels do not significantly vary across our panel of pancreatic ductal cells (0.9 to 1.2 fold-change; $p > 0.05$ for all pairwise comparisons) (Fig. 4D and E).

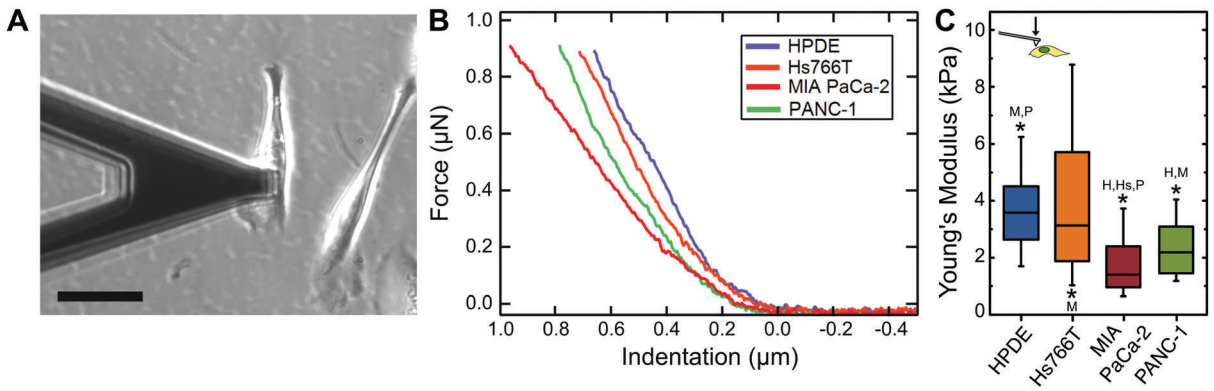

Fig. 3 Stiffness of pancreatic ductal cells. (A) Representative image of atomic force microscopy (AFM) tip over the cytoplasmic region of an HPDE cell. Scale, 40 μm. (B) Representative force curves from each cell line. Hertz–Sneddon fits are shown in Fig. S7 (ESI†). (C) Young's modulus of each cell type is measured by AFM. Stiffer cells have a larger Young's modulus than more compliant cells. $n > 28$ for all cell lines. Boxes represent the 25th and 75th percentiles, whiskers represent the 10th and 90th percentiles, and the horizontal line represents the bootstrapped median. Significance calculated by a Mann–Whitney *U* test between medians. *$p < 0.05$. The significance of pairwise comparisons between cell lines is shown in panel C by the initial(s) of the cell lines that are significantly different where H: HPDE, Hs: Hs766T, M: MIA PaCa-2, and P: PANC-1. For example, HPDE is significantly different (*$p < 0.05$) from MIA PaCa-2 (M) and PANC-1 (P).

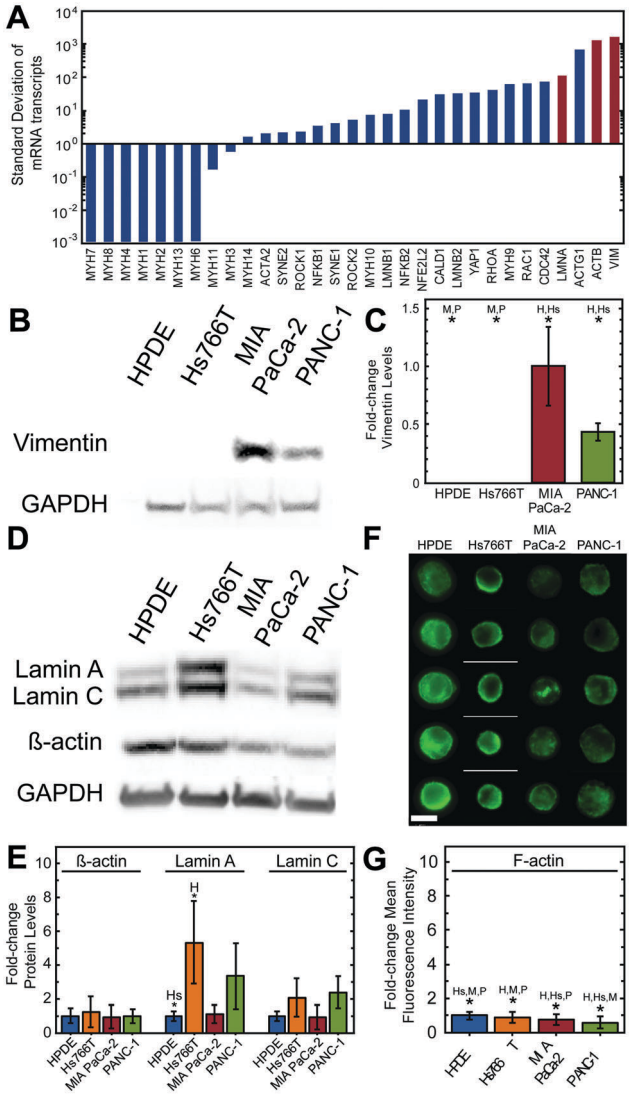

Fig. 4 Structural proteins in pancreatic ductal cell lines. (A) Bar plot showing standard deviation in expression levels of mechanoregulating genes across our three PDAC cell lines as determined by RNAseq analysis. (B) Immunoblot of vimentin and GAPDH. (C) Fold-change in protein levels compared to the MIA–PaCa2 cells, as HPDE cells show no detectable vimentin. Values are first normalized to the loading control, GAPDH. (D) Immunoblot of lamin A, lamin C, ß-actin, and GAPDH. (E) Fold-change in protein levels compared to HPDE cells. Values are first normalized to the loading control, GAPDH. (F) Imaging flow cytometry images of cells stained with phalloidin to label F-actin. Scale, 15 μm. (G) Quantification of images shows bootstrapped median fluorescence intensity of F-actin. Statistical significance for immunoblotting results is determined by a Student *t*-test. Statistical significance for imaging flow cytometry results is determined by a Mann Whitney *U* test. $*p < 0.05$. Significance is shown for cell line with the star to the cell line denoted by the initial(s). The significance of pairwise comparisons between cell lines is shown in panels C, E, and G by the initial(s) of the cell lines that are significantly different where H: HPDE, Hs: Hs766T, M: MIA PaCa-2, and P: PANC-1.

To quantify F-actin levels, we use imaging flow cytometry, which enables us to characterize large populations of single cells. While there is a slight decrease in F-actin levels for PDAC cell lines compared to the HPDE control, there is less than a 2-fold difference across our 4 pancreatic cell lines (Fig. 4F and G).

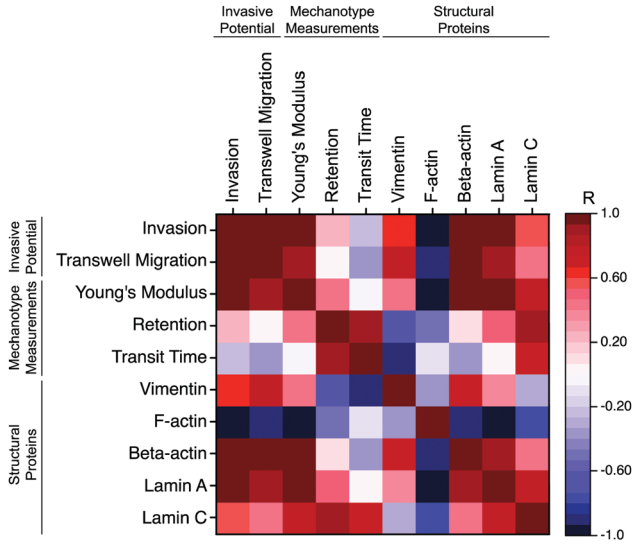

Fig. 5 Pearson's correlations (*R*) between cancer cell behaviors, mechanotype measurements, and levels of structural proteins for PDAC cells. Invasion is determined from modified scratch wound invasion assays as percent confluence at 72 hours. Transwell migration assays measure the ability of cells to migrate through 8 μm pores after 12 hours. Young's modulus is obtained using AFM. Retention is determined by PMF. Transit time is measured using microfluidic deformability cytometry. F-actin levels are measured for fixed, phalloidin-labeled cells in suspension by imaging flow cytometry. Vimentin, ß-actin, and lamin A/C levels are measured by quantitative immunoblotting. Colors are based on *R*-values that are obtained by calculating Pearson's correlation coefficients across the three cancerous PDAC cell lines (Hs766T, PANC-1, and MIA PaCa-2) in our panel.

By contrast, we observe up to a 5-fold difference in lamin A levels across our panel of cells, as measured by immunoblotting (Fig. 4D and E). Hs766T cells have the highest content of lamin A, which is approximately 5× greater than in HPDE cells (Hs766T: 5.3 ± 2.5, HPDE: 1.0 ± 0.3; $p_{\text{Hs766T–HDPE}} = 9.2 \times 10^{-2}$). The MIA PaCa-2 cells have similar lamin A levels as the HPDE control cells (MIA PaCa-2: 1.1 ± 0.5; $p_{\text{MIA–HPDE}} = 7.8 \times 10^{-1}$), while the PANC-1 cells have intermediate levels of lamin A (PANC-1: 3.3 ± 1.9; $p_{\text{PANC–HPDE}} = 1.7 \times 10^{-1}$) (Fig. 4D and E). Lamin C, which is a splice variant of lamin A, shows a much smaller ~2-fold variation across cell lines. Overall, for the three PDAC cell lines tested, our data reveal a positive trend between protein levels of lamin A and cell mechanotype ($R_{\text{LaminA–Retention}} = 0.48$, $R_{\text{LaminA–Youngs Modulus}} = 1.0$) (Fig. 5 and Table S2, ESI†). Intriguingly, we also find a positive association between lamin A and cancer cell invasion ($R_{\text{LaminA–Invasion}} = 0.96$, $R_{\text{LaminA–Transwell Migration}} = 0.90$). Taken together, our data suggest that Young's modulus and invasive behavior are more strongly associated with lamin A than with ß-actin, F-actin, or lamin C.

Discussion

More invasive PDAC cells are stiffer than less invasive PDAC cells

Across many cancer types, in both cell lines and patient samples, cancer cells that are more deformable are more invasive or have higher metastatic potential than stiffer cells.[8–17,60] By contrast, we show here that more invasive PDAC cells have a higher Young's

modulus. The Hs766T cells, which are derived from a malignant pleural effusion, are the stiffest and also the most invasive of the cell lines in our panel (Fig. 1 and 3). Of the two cell lines derived from primary tumors, PANC-1 cells are slightly more invasive and have a higher Young's modulus than MIA PaCA-2 cells. Our observations that more invasive pancreatic ductal cells tend to be stiffer suggest that the relationship between cancer cell mechanotype and invasive potential may depend on cancer type. While many studies identify more compliant breast and ovarian cancer cells as more invasive,[9,10] stiffer lung cancer and transformed skin cells have greater invasive potential.[18,19] Indeed, more invasive or metastatic cancer cell lines that generate greater traction stresses[27,61] and more contractile cells have a higher apparent stiffness.[62]

Cell mechanotype shows promise as an emerging biomarker that could be used to aid pathologists in achieving more accurate prognoses.[13,63] Our data highlight that the association between mechanotype and disease aggressiveness may vary for different tissue types. For example, while the increased deformability of breast and ovarian cancer cells may predict increased invasive behavior, our results suggest that more invasive PDAC cells could be detected or classified based on their increased stiffness. Developing a framework across different types of cancers that classifies disease aggressiveness based on cell mechanotype could provide clinically valuable information for prognosis or identifying appropriate therapeutic treatments.

An integrated understanding of cell mechanotype

Across three different mechanotype measurements, we find different trends between cell lines. Our AFM data show that the stiffest to most compliant cell lines are Hs766T = HPDE > PANC-1 > MIA PaCa-2. With PMF, we find that retention from highest to lowest is PANC-1 > Hs766T = HPDE > MIA PaCa-2. Our microfluidic deformability cytometry data show that transit times from longest to shortest are HPDE = PANC-1 > Hs766T > MIA PaCa-2. Overall we find that there is a strong, positive correlation between our microfluidic and PMF data (Fig. 5 and Table S2, ESI†). However, there is only a moderate to weak association between AFM and our fluidic assays. One possible explanation for the difference we see across methods may be a result of measuring bulk populations *versus* single cells. For example, the PANC-1 cells have a similar median transit time as the HPDE cells, but exhibit a greater range of transit times; the PANC-1 cells that have longer transit times are more likely to occlude pores in our PMF assay, and may thereby contribute to the marked increase in retention that we observe for PANC-1 compared to HPDE cells.

The different trends in cell mechanotype that we observe may also stem from the different length scales of deformation between the techniques: in our fluidic assays, cells are subject to global deformations on the order of 10 μm whereas with AFM we probe the cell with local, ~0.5 to 1 μm indentations. The deformation length scale determines which subcellular structures are primary contributors to the measured cell deformability. For example, the nucleus may dominate our fluidic deformability measurements as the nuclei of our pancreatic ductal cells have a diameter of 11 to 16 μm and the pores used in our PMF and transit time assays have a diameter of 9 to 10 μm. Therefore, the nucleus must deform in order for the whole cell to passage through a pore. As the nucleus rate-limits the transit of cells through pores much smaller than the diameter of the nucleus,[21] contributions of nuclear mechanical properties to our fluidic measurements may be more significant than the cytoskeleton. However, we observe only weak correlations between retention and transit time with levels of the nuclear envelope protein lamin A (Fig. 5 and Table S2, ESI†), suggesting that both nuclear and cytoskeletal structures may contribute to transit time and retention measurements. With AFM, we induce local deformations of the cytoplasmic region of adhered cells, thus we expect that these measurements reflect cytoskeletal architecture. We note that adhered cells also exhibit stress fibers, which can be anchored at focal adhesions where cells attach to their substrate;[25] the associated stress fibers may also contribute to the deformability of adhered cells. We note that the nucleus could additionally contribute to our AFM measurements of the cytoplasmic region. The cytoskeleton is physically connected to the nucleus through LINC protein complexes that span the nuclear envelope and interact with actin and intermediate filaments; thus, mechanical stresses applied during deformation of the cytoplasm may be transduced to the nucleus.[64]

Adhered cells can also generate intracellular tension or 'prestress' when they are attached to a Matrigel-coated substrate. As higher levels of prestress are reflected in AFM measurements of Young's modulus,[65] the increased stiffness of Hs766T cells may additionally reflect increased intracellular tension of these cells. Moreover, adhered cells are prestressed materials with actin stress fibers[66] and the nucleus under tension.[67–69] We speculate that higher levels of lamin A could also enable cells to achieve higher levels of prestress, and thereby contribute to the stiffer cytoplasmic region that we observe by AFM. Therefore, a higher density of lamin A in the nucleus could result in a smaller deformation of the cytoplasmic region for a given applied force; consistent with this, Hs766T cells have the highest levels of lamin A (Fig. 4D and E) largest Young's modulus as measured by AFM (Fig. 3C).

Given these differences between cells that are adhered *versus* suspended, as well as differences between the deformation length scales of mechanotyping techniques, such complementary methods could provide information that may be relevant in the context of distinct physical processes in metastasis and invasion, from circulation through vasculature to extravasation into distant sites. While our retention and transit time results do not strongly correlate with cell invasive potential (Fig. 5 and Table S2, ESI†), the ability of PDAC cells to passively deform may influence their ability to transit through narrow capillaries of the vasculature during metastasis. Our retention measurements may also have physiological disease relevance: it is intriguing to speculate that the occlusion of cells in micron-scale capillaries of the pulmonary bed could increase the probability that a secondary cancer site will be established.

The molecular origins of variability in cell mechanotype

Here we show that there is a 5-fold difference in lamin A protein levels across 4 pancreatic ductal cell lines. Our results also show a strong correlation between lamin A levels and Young's modulus as measured by AFM (Fig. 5 and Table S2, ESI†),

indicating that this key structural protein of the cell nucleus may contribute to the observed variability in mechanotype that we observe across the PDAC cell lines. Our results are consistent with previous findings showing that lower levels of lamin A result in more deformable cells.[21,58,70]

We also observe that cells with higher levels of lamin A tend to be more invasive (Fig. 5). For example, the Hs766T cells have the highest expression of lamin A (1.6 to 5.3-fold increase compared to the other pancreatic ductal cells lines) (Fig. 4D and E) and are the most invasive (20 to 38% higher wound confluence at 72 hours than the other pancreatic ductal cell lines, Fig. 1). These findings contrast previous studies that show increased levels of lamin A can impede the active migration and passive transit of cells through narrow pores that are ~50% smaller than the diameter of their nuclei.[21,22] However, cells with reduced levels of lamin A exhibit increased frequency of nuclear envelope rupture,[71,72] apoptosis, and cell death[22] when migrating through micron-scale pores and 3D collagen gels. Thus, while a more compliant nucleus, with lower lamin A levels, can enable changes in shape that are required for deformation through narrow gaps, a threshold level of lamin A and/or mechanical stability appears to be necessary to prevent cell death and excessive nuclear rupture events, which ultimately cause DNA damage. Further, a stiffer nucleus could provide other advantages during invasion. Because polymerizing actin bundles generate forces and push against the nucleus during invadopodia formation,[73] we speculate that a stiffer nucleus with higher levels of lamin A could provide more resistance to the forces exerted by growing invadopodia and thereby enhance the ability of cells to penetrate and invade into the surrounding matrix. Indeed, lamin A-deficient mouse embryo fibroblasts cells show reduced protrusions while migrating through a collagen matrix, as well as lower 3D migration speeds.[74] Thus, both lower and higher levels of lamin A may offer distinct advantages for cancer cells.

While lamin A appears to be implicated in the progression of some types of cancer, there is currently no consensus on the role of lamin A in cancer progression or prognosis.[75] Lamin A overexpression is correlated to increased growth and invasion in prostate cancer,[76] while reduced lamin A levels are linked to poor prognosis in gastric and squamous cell carcinoma, as well as some skin cancers.[77] The variability in mechanotype that we observe could stem from other differences between cell lines. Although the cell lines in our panel are all pancreatic ductal cells, they are derived from different sites, including primary tumors and pleural effusion. Despite their different origins, all three PDAC cell lines have mutations in *KRAS*, *TP53*, and *p16*. The Hs766T cells have an additional *SMAD4* mutation (Table S1, ESI†), which could contribute to its increased invasive potential.[78,79] In addition to these founder mutations, other genetic alterations could affect mechanotype. Future studies measuring the deformability of primary cells with well-characterized genetic mutations may address the link between genotype, mechanotype, and invasive behavior.

We also find that there is significant variability in vimentin levels across PDAC cell lines (Fig. 4B and C), and that cells with higher vimentin levels are more compliant and less invasive. This apparent discrepancy with previous mechanical studies of cells with decreased vimentin levels[50–52] may be due to the fact that we investigate endogeneous vimentin levels across different cell lines, rather than specifically manipulating vimentin levels by knockdown or overexpression. However, during epithelial-to-mesenchymal transition (EMT), cells tend to express increased levels of vimentin and become more motile and invasive;[53] our previous work shows that EMT-transformed ovarian cancer cells are more deformable than epithelial-type cells.[15] Our current study also reveals that pancreatic cancer cells with higher vimentin levels are more deformable, although they are less invasive. It will be interesting to more thoroughly investigate the role of vimentin in the mechanical properties and invasion of pancreatic cancer cells in future work.

Our bioinformatics analysis highlights additional mechanome genes that could regulate PDAC cell mechanotype. For example, we observe that components of the Rho/ROCK pathway also exhibit significant variability across PDAC cell lines. These proteins, such as RhoA, are implicated in cell contractility,[80–82] and may thus impact cancer cell invasion, response to stiffer extracellular matrices, and metastasis. Further investigations should provide deeper insight into the molecular basis of how cells regulate their mechanotype to adapt to a microenvironment of a particular stiffness, and how such changes in cell mechanotype may affect cancer behaviors, from invasion to proliferation. It is thought that more compliant cells could more easily transit narrow channels of the vasculature and metastasize to distant sites; however, stiffer cells may be better able to sustain the physical forces in the microenvironment and generate greater contractile forces that enable invasion into surrounding tissues. Such studies would also provide deeper insight into the open question of whether tumor cell mechanotype contributes to cancer progression, or is a byproduct that accompanies disease progression.

Towards clinical benefit

We anticipate that expanding our knowledge of the PDAC cell mechanome could identify novel drug targets. One of the greatest challenges in PDAC treatment is the development of effective therapies that impede metastasis, as metastatic tumor burden is thought to be responsible for over 70 percent of PDAC-related deaths.[83] Knowledge of the PDAC mechanome could provide insight into how cells alter mechanosignaling pathways in response to the stiffness of their microenvironment. Targeting the molecular components that are triggered by mechanical cues may impede cancer progression by interrupting the positive feedback loop that drives cells to generate more ECM, which results in a stiffer tumor and increases PDAC progression.[4] Insights into cell physical properties and their contributions to the complex cancer phenotype are thus urgently needed for improving the prognosis of patients with pancreatic cancer.

Experimental methods

Cell culture

The nontransformed human pancreatic ductal epithelial (HPDE) cell line is from Ming-Sound Tsao from the Department of

Laboratory Medicine and Pathobiology at the Ontario Cancer Institute (University Health Network-Princess Margaret Hospital, Toronto) and the Department of Medical Biophysics (University of Toronto, Ontario, Canada). The pancreatic ductal adenocarcinoma (PDAC) cell lines (Hs766T, MIA PaCa-2, and PANC-1) are from the American Type Culture Collection (ATCC). HPDE cells are cultured in Keratinocyte-SFM (Life Technologies) supplemented with prequalified human recombinant Epidermal Growth Factor 1-53 (Life Technologies), Bovine Pituitary Extract (Life Technologies), and 1% v/v penicillin–streptomycin (Gemini BioProducts). Hs766T, MIA PaCa-2, and PANC-1 cells are grown in high glucose, L-glutamine Dulbecco's Modified Eagle Medium (DMEM) (Life Technologies) with 10% fetal bovine serum and 1% v/v penicillin–streptomycin (Gemini BioProducts). Cells are cultured at 5% CO_2 and 37 °C.

Scratch wound invasion, migration, and proliferation assays

We perform invasion, migration, and proliferation assays using the IncuCyte time-lapse imaging system (EssenBioscience). To measure cell invasion through a 3D matrix, we perform modified scratch wound invasion assays with an overlay of Matrigel to simulate the ECM.[30,31,84] We plate cells in the wells of a 96-well plate with a thin Matrigel (100 μg ml^{-1}) layer for cell attachment at 95% confluency, create a scratch wound, overlay the scratch with a ~1.5 mm-thick layer of 8 mg ml^{-1} Matrigel (Corning), and perform time-lapse imaging using the IncuCyte Zoom (Essen Bioscience) at 5% CO_2 and 37 °C. Phase contrast images of cells are acquired every 2 hours for 120 hours. We determine the confluence of cells in the wound area at each time point using quantitative image analysis (Essen Bioscience). To assay the ability of cells to migrate on a 2D substrate, we perform this same assay without Matrigel and image every 2 hours for 72 hours. Since both scratch wound invasion and migration assays may be influenced by cell proliferation, we also measure percent confluence by sparsely plating cells (2000 cells per well of a 96-well plate) and acquiring phase contrast images every 2 hours for 120 hours. We also determine proliferation and apoptosis rates of cells with a Matrigel overlay. Cells are prepared as described above for a proliferation assay. Prior to overlay with Matrigel (8 mg ml^{-1}), cells were stained with 3 μM DRAQ7, a cell impermeable nuclear dye that only intercalates into the DNA of apoptosed cells.

Transwell migration

To assay the ability of cells to migrate through 8 μm pores, we use 24-well uncoated transwell inserts with porous polycarbonate membranes (Costar, Corning). For 1 hour prior to the experiments, we hydrate each well in serum-free DMEM media. We then load 150 μl of a suspension of 6.7×10^5 cells per ml into each well and incubate at 5% CO_2, 37 °C for 12 hours. After the incubation period, cells remaining on the top side of each membrane are removed with a cotton swab; all of the cells that have migrated to the bottom of the membrane are fixed in 100% methanol, stained with Hoechst 33342 (Life Technologies), and washed with 1× PBS (Corning). Imaging of stained cells is performed using a fluorescent microscope (Zeiss EC Plan-Neofluar 20× objective; NA 0.5/Ph2 M27). The number of cells that migrate to the bottom of the membrane is determined by counting the number of nuclei from images of the bottom membrane. Transwell migration efficiency is determined by the number of migrated cells divided by the total number of cells loaded.

Parallel microfiltration (PMF)

The PMF method is described previously in detail.[15] In brief, we assemble the device with a polycarbonate membrane that has pores of 10 μm diameter (Isopore, Millipore). To minimize cell-surface interactions, we incubate each well with 1% w/v bovine serum albumin (BSA) (Fisher Scientific) for 1 hour at 37 °C. The BSA solution is then removed and wells are air dried for at least 1 hour before each experiment. Cell suspensions are prepared at a concentration of 6.0×10^5 cells per ml and filtered through a 35 μm mesh filter to reduce the number of cell aggregates. To measure cell number and size, we use an automated cell counter (TC20, BioRad); this also confirms that over 98% of cells are single cells (Fig. S4, ESI†). Using compressed air as a pressure source, we apply 14 kPa for 50 s. We determine the percentage (%) retention by collecting the cell suspension that remains in the top well and measuring its mass using a precision balance (Northeast Scale Inc.); retention is defined as $mass_{final}/mass_{initial}$. We load samples into at least three wells per cell line per experiment, and at least ten wells over three independent experiments are measured for each cell line.

Microfluidic deformability cytometry

To evaluate the ability of single cells to passively deform through micron-scale pores, we use microfluidic devices with channels that have a smallest dimension of 9 μm × 10 μm (width × height), which we fabricate using standard soft photolithography techniques.[85] To pattern the device design onto a silicon master, SU-8 3010 negative photoresist (MicroChem) is spincoated onto a 4″ silicon wafer and exposed to UV light through a photomask. Polydimethylsiloxane (Sylgard 184 silicone elastomer, Dow Corning) is mixed with a 10 : 1 ratio of base to crosslinker, poured over the silicon master, and cured at 80 °C for 1 hour. A biopsy punch is used to create inlets and outlets. The PDMS is bonded to #1.5-thickness glass coverslips using plasma corona discharge and baked at 80 °C for 20 minutes to ensure bonding. To minimize cell-wall interactions, we add Pluronic F-127 surfactant (0.1 w/v%) (Sigma-Aldrich) to the cell suspension.[29] Cell suspensions are flowed through the microfluidic device using pressure-driven flow (10 psi).[86] We image cells that deform through the narrow channels by acquiring images at 2000 frames per second using a CMOS camera (Miro eX1, Vision Research) mounted on an inverted microscope. For each cell line, we obtain videos over three independent experiments. To determine the timescale for single cells to transit through the 9 μm constriction, or transit time, we perform post-acquisition analysis using a custom MATLAB script (Mathworks).

Atomic force microscopy (AFM)

AFM is performed using the MFP-3D-BIO system (Asylum Research, Oxford Instruments). Cells are probed with the "C"

tip of an MLCT probe (Bruker) at room temperature. The sensitivity and spring constant of each probe (11.5 to 14.5 mN m^{-1}) are calibrated before each experiment. Cells are plated on a polystyrene petri dish coated with a thin layer of Matrigel (100 μg ml^{-1}) approximately 24 hours prior to each experiment. Force curves are acquired by indenting the central cytoplasmic region of 25 to 35 cells for each cell line. To avoid possible contribution of adjacent cells, only single cells were probed. Approach and retract speeds for all experiments are 5 μm s^{-1}. The elastic modulus for each cell is determined by fitting force curves with the Hertz–Sneddon model[87,88] using Asylum Research software.

Gene expression and bioinformatics analysis

We use publicly available RNA-seq data for 41 PDAC cell lines for gene expression analysis.[46] Using STAR v.2.4.2a,[89] we align RNA sequence reads to the human reference genome (hg38) with Ensembl v.82 gene annotations. STAR is run with the following parameters: minimum/maximum intron sizes are set to 30 and 500 000; noncanonical, unannotated junctions are removed; maximum tolerated mismatches is set to 10; and the outSAMstrandField intron motif option is enabled. To quantify per-sample read abundances we use the Cuffquant command included with Cufflinks v.2.2.1,[90] with fragment bias correction and multiread correction enabled. All other options are set to default. Finally, fragments per kilobase of exon per million fragments mapped (FPKM) are calculated using the Cuffnorm command with default parameters. We use these FPKM values to compare expression levels of genes whose protein products are implicated in regulation of cell mechanical properties.[40–45] To identify the mechanoregulating genes with the highest variability in expression across PDAC cell lines, we calculate the standard deviation of mRNA levels for genes that encode proteins that are implicated in mechanotype.

Imaging flow cytometry

To visualize F-actin, cells are fixed with 4% paraformaldehyde (Sigma) in 1× PBS (Corning), permeabilized with 0.3% Triton X-100 in 1× PBS (Corning), and stained with phalloidin conjugated to AlexaFluor488 (1 : 100 in 0.3% Triton X-100 in 1× PBS; Life Technologies) at room temperature for 30 minutes. To image the nucleus, cells are stained with DRAQ5 (1 : 250 in 0.3% Triton X-100 in 1× PBS; ThermoFisher) at room temperature for 20 minutes. Images of individual cells in suspension are acquired using imaging flow cytometry (Amnis ImageStream, Millipore). Quantification of F-actin intensity, cell size, and nuclear size is conducted using the IDEAS software (Amnis, Millipore).

Western blots

Western blots are performed as previously described[21] with slight modifications. Cell lysates are prepared from 2×10^6 cells with 100 μl urea lysis buffer that has a final concentration of 9 M urea, 10 mM Tris–HCl (pH 8), 10 μM EDTA, 500 μM phenylmethylsulfonyl fluoride, 20 μl of β-mercaptoethanol (Sigma), and protease inhibitor at the suggested working concentration (cOmplete ULTRA tablets). Proteins are separated on a 4–12% Bis-Tris gel (Life Technologies) with 1× MES running buffer (Life Technologies) and then transferred to nitrocellulose membranes, blocked with 5% fat-free milk, and labeled with primary antibodies against vimentin (MS-129-P0, ThermoFisher), β-actin (MA5-15739, ThermoFisher), lamin A/C (sc-6215, Santa Cruz Biotech), and GAPDH (MA5-15738, ThermoFisher) as a loading control. Membranes are then incubated with host-specific secondary antibodies conjugated to horseradish peroxidase (HRP) (Abcam) and imaged using chemiluminescence (ThermoFisher) on a digital imaging system (AlphaImager IS-1000, Alpha Innotech Corporation). Expression levels are quantified by analysis of optical density in the linear regime using ImageJ software (National Institutes of Health).

Statistical analysis

All data are obtained from at least 3 independent experiments. For data with normal distributions, we determine statistical significance using a Student's *t*-test (Excel, Microsoft). For data that exhibit a non-normal distribution, we perform bootstrapping to obtain the bootstrapped median and confidence intervals; we then use the Mann–Whitney *U* test to determine statistically significant differences between non-normal distributions the Statistical and Machine Learning Toolbox in MATLAB (Mathworks) and Origin (OriginLab). Density scatter plots for transit time data are plotted using the dscatter function (Richard Henson, MathWorks File Exchange) in MATLAB (Mathworks).

Acknowledgements

We thank Shivani Sharma and Adam Steig for consultations on AFM and Tae-Hyung Kim for assistance with gene expression analysis and critical feedback on the manuscript. We thank James Tidball for generous use of the AlphaImager imaging system. Imaging flow cytometry was performed in the UCLA Flow Cytometry Core Facility that is supported by National Institutes of Health awards CA-16042 and AI-28697, the Jonsson Comprehensive Cancer Center, the Center for AIDS Research, and the David Geffen School of Medicine at UCLA. IncuCyte Zoom experiments were performed in facilities supported by the Eli & Edythe Broad Center of Regenerative Medicine & Stem Cell Research at UCLA and the Jonsson Comprehensive Cancer Center. We are grateful for our funding from the NSF (CAREER DBI-1254185 to ACR), the NIH/National Center for Advancing Translational Science (NCATS) (UCLA CTSI Grant Number UL1TR000124), and the Farber Family Foundation. AVN is supported by a David Geffen Scholarship and the UCLA-IBP Eureka Scholarship Fund. AHN is supported by an NIH T32 from Department of Gastroenterology (NIH GI Training Grant (T32 DK07180-37)), as well as the Gerald S. Levey Surgical Research Training Award. AMW is supported by the UCLA Undergraduate Research Scholars Program (Gottlieb Endowment) and Whitcome Summer Research Fellowship.

References

1 C. Bosetti, P. Bertuccio, E. Negri, C. La Vecchia, M. P. Zeegers and P. Boffetta, *Mol. Carcinog.*, 2012, **51**, 3–13.

2 L. Rahib, B. D. Smith, R. Aizenberg, A. B. Rosenzweig, J. M. Fleshman and L. M. Matrisian, *Cancer Res.*, 2014, **74**, 2913–2921.

3 D. T. Butcher, T. Alliston and V. M. Weaver, *Nat. Rev. Cancer*, 2009, **9**, 108–122.

4 H. Laklai, Y. A. Miroshnikova, M. W. Pickup, E. A. Collisson, G. E. Kim, A. S. Barrett, R. C. Hill, J. N. Lakins, D. D. Schlaepfer, J. K. Mouw, V. S. LeBleu, N. Roy, S. V. Novitskiy, J. S. Johansen, V. Poli, R. Kalluri, C. A. Iacobuzio-Donahue, L. D. Wood, M. Hebrok, K. Hansen, H. L. Moses and V. M. Weaver, *Nat. Med.*, 2016, **22**, 497–505.

5 F. Kai, H. Laklai and V. Weaver, *Trends Cell Biol.*, 2016, **26**, 1–12.

6 D. E. Discher, P. Janmey and Y.-L. Wang, *Science*, 2005, **310**, 1139–1143.

7 E. L. Baker, J. Lu, D. Yu, R. T. Bonnecaze and M. H. Zaman, *Biophys. J.*, 2010, **99**, 2048–2057.

8 V. Swaminathan, K. Mythreye, E. Tim O'Brien, A. Berchuck, G. C. Blobe and R. Superfine, *Cancer Res.*, 2011, **71**, 5075–5080.

9 W. Xu, R. Mezencev, B. Kim, L. Wang, J. McDonald and T. Sulchek, *PLoS One*, 2012, **7**, e46609.

10 M. H. Lee, P. H. Wu, J. R. Staunton, R. Ros, G. D. Longmore and D. Wirtz, *Biophys. J.*, 2012, **102**, 2731–2741.

11 S. E. Cross, Y.-S. Jin, J. Rao and J. K. Gimzewski, *Nat. Nanotechnol.*, 2007, **2**, 780–783.

12 T. W. Remmerbach, F. Wottawah, J. Dietrich, B. Lincoln, C. Wittekind and J. Guck, *Cancer Res.*, 2009, **69**, 1728–1732.

13 H. T. K. Tse, D. R. Gossett, Y. S. Moon, M. Masaeli, M. Sohsman, Y. Ying, K. Mislick, R. P. Adams, J. Rao and D. Di Carlo, *Sci. Transl. Med.*, 2013, **5**, 212ra163.

14 S. Byun, S. Son, D. Amodei, N. Cermak, J. Shaw, J. H. Kang, V. C. Hecht, M. M. Winslow, T. Jacks, P. Mallick and S. R. Manalis, *Proc. Natl. Acad. Sci. U. S. A.*, 2013, **110**, 7580–7585.

15 D. Qi, N. Kaur Gill, C. Santiskulvong, J. Sifuentes, O. Dorigo, J. Rao, B. Taylor-Harding, W. Ruprecht Wiedemeyer and A. C. Rowat, *Sci. Rep.*, 2015, **5**, 17595.

16 H. W. Hou, Q. S. Li, G. Y. H. Lee, A. P. Kumar, C. N. Ong and C. T. Lim, *Biomed. Microdevices*, 2009, **11**, 557–564.

17 M. Plodinec, M. Loparic, C. A. Monnier, E. C. Obermann, R. Zanetti-Dallenbach, P. Oertle, J. T. Hyotyla, U. Aebi, M. Bentires-Alj, R. Y. H. Lim and C.-A. Schoenenberger, *Nat. Nanotechnol.*, 2012, **7**, 757–765.

18 L.-S. Z. Rathje, N. Nordgren, T. Pettersson, D. Rönnlund, J. Widengren, P. Aspenström and A. K. B. Gad, *Proc. Natl. Acad. Sci. U. S. A.*, 2014, **111**, 1515–1520.

19 H. W. Yu, Y. Q. Chen, C. M. Huang, C. Y. Liu, A. Chiou, Y. K. Wang, M. J. Tang and J. C. Kuo, *J. Cell. Mol. Med.*, 2015, **19**, 934–947.

20 G. Salbreux, G. Charras and E. Paluch, *Trends Cell Biol.*, 2012, **22**, 536–545.

21 A. C. Rowat, D. E. Jaalouk, M. Zwerger, W. L. Ung, I. A. Eydelnant, D. E. Olins, A. L. Olins, H. Herrmann, D. A. Weitz and J. Lammerding, *J. Biol. Chem.*, 2013, **288**, 8610–8618.

22 T. Harada, J. Swift, J. Irianto, J. W. Shin, K. R. Spinler, A. Athirasala, R. Diegmiller, P. C. D. P. Dingal, I. L. Ivanovska and D. E. Discher, *J. Cell Biol.*, 2014, **204**, 669–682.

23 J. L. Mackay and S. Kumar, *Methods Mol. Biol.*, 2013, **931**, 313–329.

24 M. L. Rodriguez, P. J. Mcgarry and N. J. Sniadecki, *Appl. Mech. Rev.*, 2013, **65**, 1–41.

25 S. Tojkander, G. Gateva and P. Lappalainen, *J. Cell Sci.*, 2012, **125**, 1855–1864.

26 N. Wang, I. M. Tolic-Norrelykke, J. Chen, S. M. Mijailovich, J. P. Butler, J. J. Fredberg and D. Stamenovic, *Am. J. Physiol.: Cell Physiol.*, 2002, **282**, 606–616.

27 C. M. Kraning-rush, J. P. Califano and C. A. Reinhart-king, *PLoS One*, 2012, **7**, e32572.

28 E. L. Deer, J. González-Hernández, J. D. Coursen, J. E. Shea, J. Ngatia, C. L. Scaife, M. A. Firpo and S. J. Mulvihill, *Pancreas*, 2010, **39**, 425–435.

29 K. D. Nyberg, M. B. Scott, S. L. Bruce, A. B. Gopinath, D. Bikos, T. G. Mason, W. Kim, H. Sung and A. C. Rowat, *Lab Chip*, 2016, **16**, 3330–3339.

30 M. Unbekandt, D. R. Croft, D. Crighton, M. Mezna, D. Mcarthur, P. Mcconnell, A. W. Schüttelkopf, S. Belshaw, A. Pannifer, M. Sime, J. Bower, M. Drysdale and M. F. Olson, *Cell Commun. Signaling*, 2014, **12**, 1–15.

31 M. Kobayashi, C. Salomon, J. Tapia, S. E. Illanes, M. D. Mitchell and G. E. Rice, *J. Transl. Med.*, 2014, **12**, 1–12.

32 K. Nabeshima, T. Inoue, Y. Shimao and T. Sameshima, *Pathol. Int.*, 2002, **52**, 255–264.

33 X. Zhao, S. Gao, W. Sun, H. Zhang, J. Sun, S. Yang and J. Hao, *Cancer Res.*, 2014, **74**, 2455–2464.

34 C. Ma, B. Wu, X. Huang, Z. Yuan, K. Nong, B. Dong, Y. Bai, H. Zhu, W. Wang and K. Ai, *Tumor Biol.*, 2014, **35**, 12729–12735.

35 M. H. Zaman, L. M. Trapani, A. L. Sieminski, D. Mackellar, H. Gong, R. D. Kamm, A. Wells, D. A. Lauffenburger and P. Matsudaira, *Proc. Natl. Acad. Sci. U. S. A.*, 2006, **103**, 15–16.

36 V. Ellenrieder, B. Alber, U. Lacher, S. F. Hendler, A. Menke, W. Boeck, M. Wagner, M. Wilda, H. Friess, M. Büchler, G. Adler and T. M. Gress, *Int. J. Cancer*, 2000, **85**, 14–20.

37 T. Fujisawa, B. Rubin, A. Suzuki, P. S. Patel, W. A. Gahl, B. H. Joshi and R. K. Puri, *PLoS One*, 2012, **7**, 1–10.

38 A. Haage and I. C. Schneider, *FASEB J.*, 2014, **28**, 3589–3599.

39 M. J. Rosenbluth, W. A. Lam and D. A. Fletcher, *Lab Chip*, 2008, **8**, 1062–1070.

40 T. P. Stossel and J. H. Hartwig, *Cell*, 2003, **4**, 444–445.

41 R. McBeath, D. M. Pirone, C. M. Nelson, K. Bhadriraju and C. S. Chen, *Dev. Cell*, 2004, **6**, 483–495.

42 A. Cuadrado, Z. Martín-Moldes, J. Ye and I. Lastres-Becker, *J. Biol. Chem.*, 2014, **289**, 15244–15258.

43 A. J. Engler, S. Sen, H. L. Sweeney and D. E. Discher, *Cell*, 2006, **126**, 677–689.

44 W. Zhang, K. Kai, D. S. Choi, T. Iwamoto, Y. H. Nguyen, H. Wong, M. D. Landis, N. T. Ueno, J. Chang and L. Qin, *Proc. Natl. Acad. Sci. U. S. A.*, 2012, **109**, 18707–18712.

45 J. Swift, I. L. Ivanovska, A. Buxboim, T. Harada, P. C. D. P. Dingal, J. Pinter, J. D. Pajerowski, K. R. Spinler, J.-W. Shin, M. Tewari,

F. Rehfeldt, D. W. Speicher and D. E. Discher, *Science*, 2013, **341**, 1240104.
46 J. Barretina, G. Caponigro, N. Stransky, K. Venkatesan, A. A. Margolin, S. Kim, C. J. Wilson, J. Lehár, G. V. Kryukov, D. Sonkin, A. Reddy, M. Liu, L. Murray, M. F. Berger, J. E. Monahan, P. Morais, J. Meltzer, A. Korejwa, J. Jané-Valbuena, F. A. Mapa, J. Thibault, E. Bric-Furlong, P. Raman, A. Shipway, I. H. Engels, J. Cheng, G. K. Yu, J. Yu, P. Aspesi, M. de Silva, K. Jagtap, M. D. Jones, L. Wang, C. Hatton, E. Palescandolo, S. Gupta, S. Mahan, C. Sougnez, R. C. Onofrio, T. Liefeld, L. MacConaill, W. Winckler, M. Reich, N. Li, J. P. Mesirov, S. B. Gabriel, G. Getz, K. Ardlie, V. Chan, V. E. Myer, B. L. Weber, J. Porter, M. Warmuth, P. Finan, J. L. Harris, M. Meyerson, T. R. Golub, M. P. Morrissey, W. R. Sellers, R. Schlegel and L. A. Garraway, *Nature*, 2012, **483**, 603–607.
47 L. Kreplak and D. Fudge, *BioEssays*, 2007, **29**, 26–35.
48 E. Gladilin, P. Gonzalez and R. Eils, *J. Biomech.*, 2014, **47**, 2598–2605.
49 M. G. Mendez, S.-I. Kojima and R. D. Goldman, *FASEB J.*, 2010, **24**, 1838–1851.
50 B. Eckes, D. Dogic, E. Colucci-guyon, N. Wang, A. Maniotis, D. Ingber, A. Merckling, F. Langa, M. Aumailley, A. Delouvée, V. Koteliansky, C. Babinet and T. Krieg, *J. Cell Sci.*, 1998, **111**, 1897–1907.
51 D. Stamenovic and N. Wang, *Am. J. Physiol.: Cell Physiol.*, 2000, **2115**, 188–194.
52 C. Liu, H. Lin, M. Tang and Y. Wang, *Oncotarget*, 2015, **6**, 15966–15983.
53 K. Vuoriluoto, H. Haugen, S. Kiviluoto, J. Mpindi, J. Nevo, C. Gjerdrum, C. Tiron, J. B. Lorens and J. Ivaska, *Oncogene*, 2010, **30**, 1436–1448.
54 H. Yamaguchi and J. Condeelis, *Biochim. Biophys. Acta, Mol. Cell Res.*, 2007, **1773**, 642–652.
55 M. Olson and E. Sahai, *Clin. Exp. Metastasis*, 2009, **26**, 273–287.
56 C. Guo, S. Liu, J. Wang, M. Z. Sun and F. T. Greenaway, *Clin. Chim. Acta*, 2013, **417**, 39–44.
57 T. Dechat, K. Pfleghaar, K. Sengupta, T. Shimi, D. K. Shumaker, L. Solimando and R. D. Goldman, *Genes Dev.*, 2008, **22**, 832–853.
58 J. Lammerding, P. C. Schulze, T. Takahashi, S. Kozlov, T. Sullivan, R. D. Kamm, C. L. Stewart and R. T. Lee, *J. Clin. Invest.*, 2004, **113**, 370–378.
59 L. A. Lautscham, C. Kammerer, J. R. Lange, T. Kolb, C. Mark, A. Schilling, P. L. Strissel, R. Strick, C. Gluth, A. C. Rowat, C. Metzner and B. Fabry, *Biophys. J.*, 2015, **109**, 900–913.
60 D. B. Agus, J. F. Alexander, W. Arap, S. Ashili, J. E. Aslan, R. H. Austin, V. Backman, K. J. Bethel, R. Bonneau, W.-C. Chen, C. Chen-Tanyolac, N. C. Choi, S. A. Curley, M. Dallas, D. Damania, P. C. W. Davies, P. Decuzzi, L. Dickinson, L. Estevez-Salmeron, V. Estrella, M. Ferrari, C. Fischbach, J. Foo, S. I. Fraley, C. Frantz, A. Fuhrmann, P. Gascard, R. A. Gatenby, Y. Geng, S. Gerecht, R. J. Gillies, B. Godin, W. M. Grady, A. Greenfield, C. Hemphill, B. L. Hempstead, A. Hielscher, W. D. Hillis, E. C. Holland, A. Ibrahim-Hashim, T. Jacks, R. H. Johnson, A. Joo, J. E. Katz, L. Kelbauskas, C. Kesselman, M. R. King, K. Konstantopoulos, C. M. Kraning-Rush, P. Kuhn, K. Kung, B. Kwee, J. N. Lakins, G. Lambert, D. Liao, J. D. Licht, J. T. Liphardt, L. Liu, M. C. Lloyd, A. Lyubimova, P. Mallick, J. Marko, O. J. T. McCarty, D. R. Meldrum, F. Michor, S. M. Mumenthaler, V. Nandakumar, T. V. O'Halloran, S. Oh, R. Pasqualini, M. J. Paszek, K. G. Philips, C. S. Poultney, K. Rana, C. A. Reinhart-King, R. Ros, G. L. Semenza, P. Senechal, M. L. Shuler, S. Srinivasan, J. R. Staunton, Y. Stypula, H. Subramanian, T. D. Tlsty, G. W. Tormoen, Y. Tseng, A. van Oudenaarden, S. S. Verbridge, J. C. Wan, V. M. Weaver, J. Widom, C. Will, D. Wirtz, J. Wojtkowiak and P.-H. Wu, *Sci. Rep.*, 2013, **3**, 1449.
61 M. J. Paszek, N. Zahir, K. R. Johnson, J. N. Lakins, G. I. Rozenberg, A. Gefen, C. A. Reinhart-king, S. S. Margulies, M. Dembo, D. Boettiger, D. A. Hammer and V. M. Weaver, *Cancer Cell*, 2005, **8**, 241–254.
62 D. Stamenovic and M. F. Coughlin, *J. Theor. Biol.*, 1999, **201**, 63–74.
63 D. R. Gossett, H. T. K. Tse, S. A. Lee, Y. Ying, A. G. Lindgren, O. O. Yang, J. Rao, A. T. Clark and D. Di Carlo, *Proc. Natl. Acad. Sci. U. S. A.*, 2012, **109**, 7630–7635.
64 A. Maniotis, C. S. Chen and D. Ingber, *Proc. Natl. Acad. Sci. U. S. A.*, 2000, **94**, 849–854.
65 C. Y. Park, D. Tambe, A. M. Alencar, X. Trepat, E. H. Zhou, E. Millet, J. P. Butler and J. J. Fredberg, *Am. J. Physiol.: Cell Physiol.*, 2010, **298**, 1245–1252.
66 S. Kumar, I. Z. Maxwell, A. Heisterkamp, T. R. Polte, T. P. Lele, M. Salanga, E. Mazur and D. E. Ingber, *Biophys. J.*, 2006, **90**, 3762–3773.
67 S. Hu, J. Chen, J. P. Butler and N. Wang, *Biochem. Biophys. Res. Commun.*, 2005, **329**, 423–428.
68 A. Mazumder and G. V. Shivashankar, *J. R. Soc., Interface*, 2010, **7**, S321–S330.
69 H. Lee, W. J. Adams, P. W. Alford, M. L. Mccain, A. W. Feinberg, S. P. Sheehy, J. A. Goss and K. K. Parker, *Exp. Biol. Med.*, 2015, **240**, 1543–1554.
70 J. L. V. Broers, E. A. G. Peeters, H. J. H. Kuijpers, J. Endert, C. V. C. Bouten, C. W. J. Oomens, F. P. T. Baaijens and F. C. S. Ramaekers, *Hum. Mol. Genet.*, 2004, **13**, 2567–2580.
71 C. M. Denais, R. M. Gilbert, P. Isermann, A. L. Mcgregor, M. Lindert, B. Weigelin, P. M. Davidson, P. Friedl, K. Wolf and J. Lammerding, *Science*, 2016, **352**, 353–358.
72 M. Raab, M. Gentili, H. De Belly, H. Thiam, P. Vargas, A. J. Jimenez, F. Lautenschlaeger, R. Voituriez, N. Manel and M. Piel, *Science*, 2016, **352**, 359–362.
73 O.-Y. Revach, A. Weiner, K. Rechav, I. Sabanay, A. Livne and B. Geiger, *Sci. Rep.*, 2015, **5**, 9466.
74 S. B. Khatau, R. J. Bloom, S. Bajpai, D. Razafsky, S. Zang, A. Giri, D. Hodzic and D. Wirtz, *Sci. Rep.*, 2012, **488**, 1–11.
75 J. I. De las Heras, D. G. Batrakou and E. C. Schirmer, *Semin. Cancer Biol.*, 2013, **23**, 125–137.
76 L. Kong, G. Schäfer, H. Bu, Y. Zhang, Y. Zhang and H. Klocker, *Carcinogenesis*, 2012, **33**, 751–759.

77 M. Prokocimer, M. Davidovich, M. Nissim-Rafinia, N. Wiesel-Motiuk, D. Z. Bar, R. Barkan, E. Meshorer and Y. Gruenbaum, *J. Cell. Mol. Med.*, 2009, **13**, 1059–1085.
78 S. Zhao, Y. Wang, L. Cao, M. M. Ouellette and J. W. Freeman, *Int. J. Cancer*, 2010, **127**, 2076–2087.
79 Y.-W. Chen, P.-J. Hsiao, C.-C. Weng, K.-K. Kuo, T.-L. Kuo, D.-C. Wu, W.-C. Hung and K.-H. Cheng, *BMC Cancer*, 2014, **14**, 181.
80 M. Amano, M. Nakayama and K. Kaibuchi, *Cytoskeleton*, 2010, **67**, 545–554.
81 S. Sharma, C. Santiskulvong, J. Rao, J. K. Gimzewski and O. Dorigo, *Integr. Biol.*, 2014, **6**, 611–617.
82 I. Aifuwa, A. Giri, N. Longe, S. H. Lee, S. S. An and D. Wirtz, *Oncotarget*, 2015, **6**, 30516–30531.
83 S. Yachida, S. Jones, I. Bozic, T. Antal, R. Leary, B. Fu, M. Kamiyama, R. H. Hruban, J. R. Eshleman, M. A. Nowak, V. E. Velculescu, K. W. Kinzler, B. Vogelstein and C. A. Iacobuzio-Donahue, *Nature*, 2010, **467**, 1114–1117.
84 C. A. Sartorius, C. T. Hanna, B. Gril, H. Cruz, N. J. Serkova, K. M. Huber, P. Kabos, T. B. Schedin, V. F. Borges, P. S. Steeg and D. M. Cittelly, *Oncogene*, 2015, **35**, 2881–2892.
85 D. C. Duffy, J. C. McDonald, O. J. A. Schueller and G. M. Whitesides, *Anal. Chem.*, 1998, **70**, 4974–4984.
86 D. J. Hoelzle, B. A. Varghese, C. K. Chan and A. C. Rowat, *J. Visualized Exp.*, 2014, **91**, e51474.
87 I. N. Sneddon, *Int.J. Eng. Sci.*, 1965, **3**, 47–57.
88 V. M. Laurent, S. Kasas, A. Yersin, T. E. Schäffer, S. Catsicas, G. Dietler, A. B. Verkhovsky and J.-J. Meister, *Biophys. J.*, 2005, **89**, 667–675.
89 A. Dobin, C. A. Davis, F. Schlesinger, J. Drenkow, C. Zaleski, S. Jha, P. Batut, M. Chaisson and T. R. Gingeras, *Bioinformatics*, 2013, **29**, 15–21.
90 C. Trapnell, B. A. Williams, G. Pertea, A. Mortazavi, G. Kwan, M. J. van Baren, S. L. Salzberg, B. J. Wold and L. Pachter, *Nat. Biotechnol.*, 2010, **28**, 511–515.